Using horizontal sonic crystals to reduce the aeroacosutic signature of a simplified ICE3 train model

(article starts on next page)

Using horizontal sonic crystals to reduce the aeroacosutic signature of a simplified ICE3 train model

G. Minelli [a],*, H.-D. Yao [a], N. Andersson [a], D. Lindblad [a], J. Forssén [b], P. Höstmad [b], S. Krajnović [a]

[a] Mechanics and Maritime Sciences, Chalmers University of Technology, Gothenburg, Sweden
[b] Applied Acoustic, Chalmers University of Technology, Gothenburg, Sweden

ABSTRACT

The design of noise barriers for high-speed trains is challenging due to the flow interaction between the train body and barriers. A failed design could affect the flow that in turn introduces additional aerodynamic loads to the train and generates extra noise. This study is the first investigation to numerically explore the detailed effects of noise barriers on high-speed trains. In particular, horizontal sonic crystals are compared to vertical, closed at the ground barriers in order to investigate the detailed effects of different noise screens on high-speed trains. The compressible IDDES is used to simulate the flow. The focus of this study is twofold. The first is to test if an alternative barrier typology can effectively reduce the noise signature, without having an impact on the train's aerodynamic performance. The second is to explore the connection between the near-field velocity fluctuations and the far-field noise. A few specific tonal frequency components have been commonly reported but not clearly explained in the literature. It is unclear if the specific tonal components are less dependent on the Reynolds numbers, although, in general, energetic flow structures are dependent on inflow speeds. Concerning the noise reduction, the results show that the sonic crystal barrier case has a significantly better performance. A modal analysis is used to explore the causes of the tonal peaks and the association of the underbody swirling vortices to the far-field noise is described.

1. Introduction

Cars are limited to a speed of 130 km/h while airplanes fly at a cruise speed of 850 km/h. Considering a three-hours travel, one can comfortably drive 350 km distance, while using the same time (without counting check-in/check-out times), an airplane can cover more than 2500 km. The wide gap between these two distances can potentially be covered by high-speed train (HST) connections. In addition, train transportation has a lower environmental impact, often connects city centres and avoids check-in/check-out times. Nevertheless, the present HST technology has not yet resolved all potential comfort and safety related issues associated with speeds in the range 400–600 km/h. An important challenge associated with this speed range resides in the aerodynamic and aeroacoustic optimization of a mean of transport originally designed for a much lower cruise speed.

The body of literature addressing train aerodynamics is vast and it has increased exponentially in the past decade. To cite but a few of the most prominent studies, the experimental work of Baker

[1,2], Bell et al. [3–5], and the computational work of Krajnović et al. [6–10] significantly contributed to develop guidelines for train manufacturers and aerodynamic advancements. Some examples of the topics that have been addressed in the works mentioned above are the ballast flight phenomenon, the description of the wake and slipstream and the effect of side wind.

On the aeroacoustics side, the progress has been slower. An aeroacoustic calculation typically requires much larger computer power and experiments require sophisticated measurement techniques and specifically designed wind tunnels. Few research groups experimentally investigated the noise signature of full scale HST models [11–13], scaled HST models [14,15] and single HST components [16]. On the computational aeroacoustic (CAA) side, even fewer studies have been carried out, mostly focusing on single part components [17–19], and in a recent study a truncated single-car train model [20] was investigated.

The present work on the aeroacoustics of train noise barriers is an extension to the aforementioned study on a truncated single car train model [20]. In that previous investigation, the authors confirmed the presence of acoustic tonal peaks found in a previous experimental activity [15], and proposed a visualization of the acoustic response of different surfaces. In the present work, the

truncated train car is extended to a full one, creating a more realistic case. The bogie cavity has been filled, not only to simplify the model and reduce the computational cost, but also to recreate a modern streamlined geometry which nowadays are commonly characterized by bogie fairings [8] and covered cavities to boost the aerodynamic performance. Two aspects that were not investigated in the previous study [20], but they are addressed in the present work, are the Reynolds number (Re) effect, from both an aerodynamics and aeroacoustics prospective, and the presence of noise barriers to mitigate the acoustic pollution generated by a train pass-by.

The paper is organized as follows: the HST model and the different barrier configurations are described in Section 2. The results are presented in Section 3, showing the effects of the Re and the acoustic barriers. Moreover, a modal analysis is used to explain the correlation between near-field flow structures and the far-field noise signature. Conclusions are drawn in Section 4.

2. Case description and numerics

2.1. Numerical setup

The main purpose of this study is to identify the acoustic signature of a HST pass-by. From the literature, it is found that the main contribution to the flow-induced noise is the interaction of the flow with the head part of the train. Therefore, a single full car body of a streamlined ICE3 train model is placed in a simple numerical domain as visualized in Fig. 1(a). The main dimensions are reported in terms of the train's width $W = 0.12$ m, the train's car length $L = 7.33W$ and its height $H = 1.2W$ in Fig. 1(b). The origin of the coordinate system is placed as in Fig. 1(c), on the symmetry line of the train model and at the centre of the gap between the ground and the train under-body. The gap between the train and the ground is $G = 0.1W$ and a sampling plane is placed at $z = 0$ (at the centre of the gap) to monitor the underbody flow, Fig. 1(c). For clarity, the gap between the ground and the model is chosen by considering the presence of a standard bogie group touching the ground surface. The bogie has been later removed in order to simplify the geometry and save computational resources. The model is a 1:25 scaled model, this factor will be used later to give an estimate of the real frequency produced by a train pass-by. Thus, all frequencies that will be discussed later in the paper will be scaled accordingly. This will be provided in Section 3.

The far-field noise is evaluated using the Ffowcs Williams-Hawkings (FW-H) analogy, see Section 2.3. For doing this, permeable surfaces are placed around the train model, as shown in Fig. 1(d). The surfaces are carefully placed outside the turbulent region to prevent artificial noise, generated by cutting off vortices at the permeable surfaces. The back surface, behind the train's tail, is excluded from the far-field calculation to avoid the artificial noise contribution of the turbulent wake. Therefore, only the side, top and front surfaces around the train are taken into consideration for the far-field noise calculation. This open-surface methodology was successfully used in previous bluff body flow analysis [18,21] showing the negative influence of a surface immersed in a turbulent wake. More evidence of the small error introduced by collecting wave pressure data on an open surface is shown in Refs. [22,23]. In these works was found that the downstream closing surface only gives a negligible contribution to the radiated sound if two conditions apply: the main noise source lays within the streamwise extension of the side surfaces and the line connecting the receivers, and the noise source is sufficiently far from the open-surface. These two conditions both apply in the present case.

Two different noise barrier configurations are chosen for the study, as shown in Fig. 2. The first one, named barrier A, is formed by a low, vertical wall placed at the two sides of the train model as shown in Fig. 2(a). A's height is chosen as low as possible, in order to cover the noise generated by the turbulent structures formed underneath the train, while affecting its aerodynamics to the minimum. The second configuration, barrier B, is inspired by so called sonic crystals, positioned longitudinally along the train as shown in Fig. 2(b). Citing [24], these screens "are formed by arrangements of acoustic scatterers in air, and provide a new and different mechanism in the fight against noise from those of the classical screens". The first sonic crystal screen was theorized by Kushwaha [25] and a description of the first experimental prototype is reported in Ref. [26]. Since then, this technology has evolved with different studies. For example their distribution and size were investigated in Ref. [27,28], and a possibility to adapt their lattice for different needs was proposed in Ref. [29]. In contrast to barrier A, barrier B allows the flow structures generated by the train's pass-by to escape between the cylinders. The escaping effect brings a very small influence to the train's aerodynamics and lowers the loads on the screen structures. Moreover, the two configurations lead to significant differences in terms of acoustic response. The advantages and disadvantages of the two barriers will be discussed in Section 3.

The sides, the inlet and the outlet boundaries are set to non-reflective free-stream boundary conditions (BC) for which the
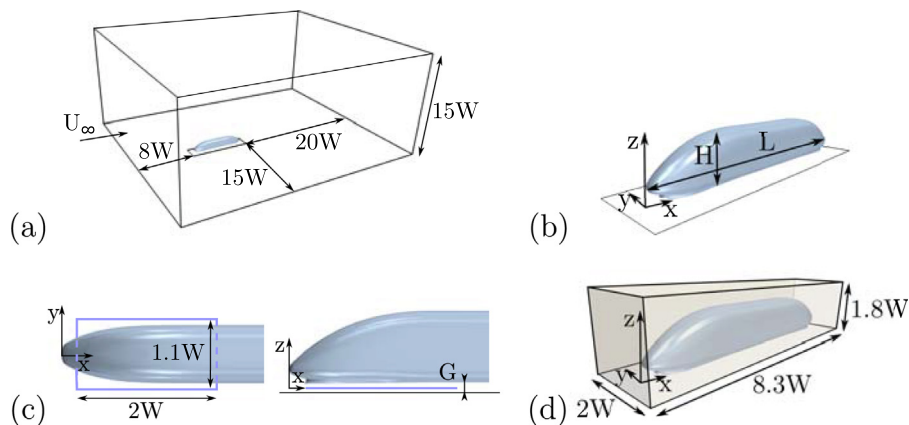

Fig. 1. The domain, the train model and the permeable surfaces for the far-field noise. (a) Size of the numerical domain. W is the width of the train. (b) Size of the one-car train model. (c) The sampling plane used for the underbody flow (in blue) placed at $z = 0$. (d) Position of the permeable surfaces around the model. (For interpretation of the references to color in this figure legend, the reader is referred to the web version of this article.)
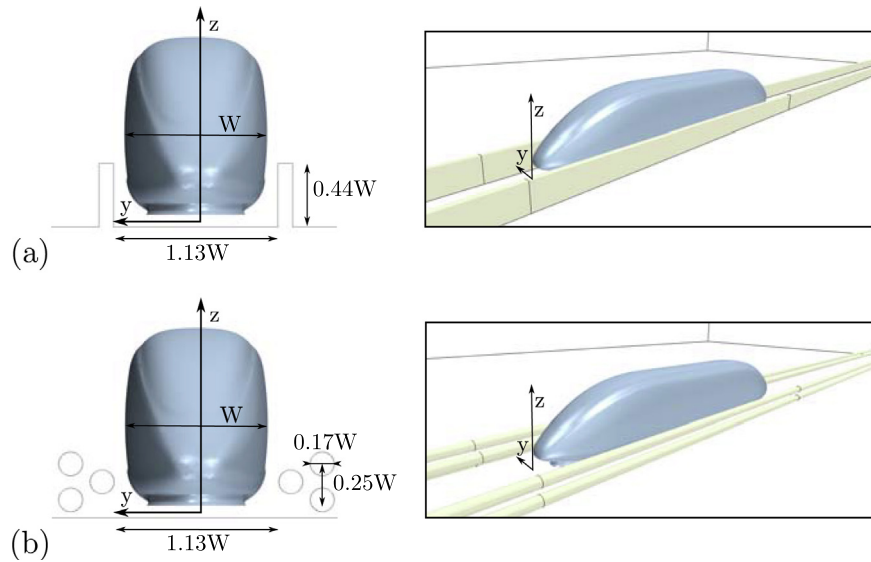
Fig. 2. Visualization of two noise barrier configurations. (a) Low and solid barriers (barrier *A*). (b) Cylindrical barriers inspired by sonic crystals (barrier *B*).

desired Mach number *M* is specified for each simulation. An appropriate mesh coarsening procedure toward the boundary and the far distance of the boundaries from the body effectively damps any unwanted reflection of acoustic pressure waves. In this way, the turbulent structures dissipate before they meet the boundaries. In addition, a sponge zone is set $3H$ upstream the outlet. The ground and the barriers are treated as moving walls, using the same velocity set at the inlet. Three *Re* are chosen for this study: $153\,000$, $230\,000$ and $307\,000$. At these Reynolds numbers, the flow is fully turbulent and the simulations are characterized by low Mach numbers: 0.06, 0.09 and 0.12, respectively. Moreover, it is reasonable to assume that the coefficients of aerodynamic forces are Reynolds number independent after $Re = 250\,000$, as reported by the European committee for standardization [30]. For clarity, *Re* is here calculated based on the incoming velocities $U_\infty = [20; 30; 40]$ m/s of the flow, the width of the train *W* and the dynamic viscosity of the flow $v = 1.569 \times 10^{-5}$ m²/s, according to the formula $Re = U_\infty W / v$.

2.2. Turbulence modelling and numerical scheme

The simulations are performed with the commercial software STAR-CCM+, version 13.06.11 [31]. The hybrid IDDES [32] turbulence model, based on the one-equation Spalart–Allmaras model [33], is used to simulate the flow field around the train model. Many studies have shown the fidelity of this methodology when applied to similar HST related incompressible (e.g., [34–36]) and mildly compressible [20] turbulent flows. Following up the work described in [20], the same method is used for a low Mach case defined within the compressible Navier–Stokes equations. Regarding the numerical schemes, a second-order implicit scheme is used for the time advancement, while a hybrid second-order-upwind/bounded-central-differencing scheme is employed for the spatial discretization. The blending factor σ, defining the percentage of use of the two schemes, is set to 0.15 allowing an 85% of the central differencing scheme for a less dissipative resolution of the flow. For further turbulence model related details, the reader is referred to Ref. [32]. The chosen time step $\Delta t_{\mathrm{m}} = 7.5 \times 10^{-6}$ s ($\Delta t_{\mathrm{m}}^* = \Delta t_{\mathrm{m}} U_\infty / H = 1.25 \times 10^{-3}$), further gives a convective Courant-Friedrichs-Lewy (CFL) number well below unity. For the highest Reynolds number, a lower time step $\Delta t_{\mathrm{m}} = 6.0 \times 10^{-6}$ is

chosen to preserve a CFL number lower than unity. The chosen time step gives a Nyquist frequency which is one order of magnitude larger than the frequency range of interest. The choice of the time step is documented in Ref. [20] where a time-independence study was performed for a similar model simulated at similar *Re*. Once the turbulent flow was fully developed, the flow was averaged over 0.3 s, which corresponds to about 30 convection cycles over the front part of the train model ($4W$ from the tip nose downwards). Concerning the meshing procedure, the built-in mesh generation tool of STAR-CCM+ has been used. More specifically, a trimmed unstructured mesh is used. The front part of the train underbody is incorporated in a refinement box to ensure an uniform cell distribution. This is done in order to preserve the acoustic information generated by pressure fluctuations and to accurately resolve a wide range of turbulent flow structures. In particular, the mesh guarantees a non-dimensional wall normal distance $n_{\max}^+ < 1$ on the entire train surface, while the maximum normalized resolution in spanwise direction $\Delta s_{\max}^+$ and in streamwise direction $\Delta l_{\max}^+$ are lower than 75. The grid independence as well as the time step independence study were performed in Ref. [20]. As a consequence, the previously selected mesh resolution is also chosen for the present work.

2.3. Far-field acoustic

The formulation 1A by Farassatt [37], for a porous, stationary integral surface, is used. The FW-H solver in STAR-CCM+ implements the advanced time approach for subsonic flows, to account for the time delay between the emission time and reception time at the receiver [38]. For the simulations presented in this work, the sampling of the pressure, density and velocity fluctuations over the permeable surfaces is performed over a 0.3 s period. Specifically, the variables are sampled every time step for a total of $40\,000$ samples. The sound pressure level (SPL) plots were obtained with the Hanning window function, with a window length of 4000 samples (19 analysis blocks) and a 50% overlap between blocks, leading to a frequency resolution of 1 Hz. Noteworthy is to mention that no energy or amplitude scaling [39] is performed on the presented results for two main reasons. The first one is that the model is scaled, therefore does not reproduce the real level of a full scale geometry. Secondly, the results presented here are only used in a comparative manner between the outcome of different cases.

2.4. Modal analysis

Proper orthogonal decomposition (POD) is used for the modal analysis of the underbody flow field. The POD provides an in-depth understanding of flow structures in terms of both energy contents and characteristic frequencies. The POD performed in this work, is made using velocity components snapshots taken from the plane shown in Fig. 1(c). As originally proposed in [40], and later introduced with the method of snapshots in [41], this method is based on the energy ranking of orthogonal structures computed from a correlation matrix of the snapshots. A singular value decomposition (SVD) approach is used to conduct the POD analysis over 1000 snapshots. The time step between CFD snapshots is $\Delta t_s = 7.5 \times 10^{-5}$ s. Thus, the highest frequency considered in the modal analysis (the Nyquist frequency) is 6667 Hz. The lowest frequency captured is limited by the snapshot total sampling time to 132 Hz (the snapshots are collected over 0.075 s and at least ten periods should be captured for a reliable frequency evaluation). These two frequencies, as divided by a factor of 25, give a reliable POD real frequency range between 5.3–267 Hz. The present method was successfully used in previously published work by the same authors [42–44]. Here, the method is used to characterize the dynamics of the velocity field and, based on their energy content, identify flow structures that contribute to far-field noise peaks. In particular, the POD is applied with a zonal approach. In this way, the frequency content of the considered field portion can be extracted and isolated. After this, the frequency peaks of the flow structures are compared to the far-field noise peaks in order to find possible correlations.

3. Results

This section is divided into three parts. In the first one, the aeroacoustic characterization of the noise barriers' effect in the far-field is reported. The noise signature of each barrier case at different Re is discussed by the use of spectral analysis, sound pressure level (SPL) and overall sound pressure level (OASPL) graphs to identify the main noise sources and their directivities. The second part describes the cases from a global aerodynamic point of view in terms of forces and flow structures. The last part of this section aims to emphasise the description of the flow structures arising in the underbody region, supposedly responsible for the main tonal peak in the acoustic signal. Therefore, a modal analysis is performed on both streamwise and spanwise velocity components to better describe the flow and possibly associate the far-field noise to the near-field flow structures.

3.1. Barriers and Reynolds number dependency. Noise characterization

A total of 54 receivers are distributed on three arches that surround the train model along the streamwise direction, as displayed in Fig. 3. For brevity, only half of the arches and only every third receiver are depicted. The arches are located at

$x = 0W$, $x = 1.67W$ and $x = 3.33W$, while the distance of the receivers from the x axis $r = 3.33W$. The SPL and OASPL values at these receivers are calculated based on pressure data obtained from the acoustic analogy based on the FW-H equation for a permeable surface described earlier. Note that this permeable surface contains the barriers. Therefore, the computation of the far-field noise takes into account the noise reduction brought by these solid screens.

As discussed earlier, a scaling factor 25 is applied to every SPL spectrum in order to visualize the frequencies in a full-scale context. The SPL spectra in Figs. 4 and 5 are further scaled with the A-weighting function. Each spectrum curve shown in the mentioned figures represents the averaged spectrum over all receivers, for each simulation. Isolating the Re effect for all different cases, we can notice a steady increase with the increasing velocity (or Mach numbers), as shown in Fig. 4 and Table 1. In particular, considering the non-barrier case, the averaged SPL increase (between the low and high Re cases) is 24 dB, in line with the experimental value reported in Ref. [15]. Considering the same quantity, a 15 dB overall noise increase for barrier A and 20 dB for barrier B are reported in Table 1. The presence of the barriers somehow mitigates the overall growth of noise with increasing flow speed. From the same table, one can notice that barrier A only is beneficial at high Re, when the full frequency range is considered. In contrast to that, barrier B shows a consistent reduction of the overall noise level for the range of the Reynolds numbers used. Analysing the spectra in Fig. 4, one can notice the presence of a tonal peak at 135 Hz across all cases and for all Re. As will be discussed later in Section 3.2, this peak seems to be closely connected to the swirling vortices generated in the underbody region. Increasing the speed, one can also notice that superharmonics of this tonal component start to occur in the spectra. Considering Fig. 4(b), the presence of a broader acoustic peak at 48 Hz is observed. This peak remains constant in frequency when increasing the inflow speed. This suggests the presence of a standing acoustic wave, whose half wavelength fits into the distance between the left and right screen (1.13W in Fig. 1(a)) according to the formula $f = c/(2L)$, where c is the speed of sound and L the barrier distance. Nevertheless, compared to the overall SPL level, this peak decreases in amplitude with increasing speed, being covered by a broader and more energetic spectrum generated by a higher-Re turbulent flows.

In Fig. 5, the frequency domain has been divided into three bands, $B1$, $B2$ and $B3$, each of which represents the bounds used in the OASPL calculations. The frequency bands are chosen based on the noise spectral characteristics. The $B1$ region contains the lowest frequencies which are still relevant for building acoustic propagation. $B2$ contains the tonal peak and the frequency range which is most important for the acoustic propagation into buildings, while $B3$ collects the highest frequencies captured, which are not critical for the acoustic propagation and which show a limited difference between different cases. One can notice that the A-weighting filter acts principally on low frequencies, lowering the perceived acoustic levels in region $B1$. Region $B2$ is the one with the highest noise peak at 135 Hz, previously mentioned. Region
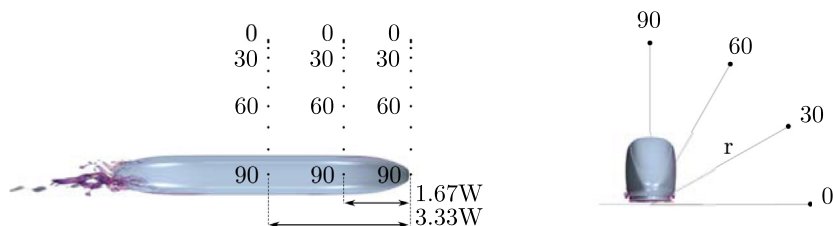

Fig. 3. Location of the receivers. Three arches are positioned along the streamwise direction. For brevity, only half of the receiver arches are represented.
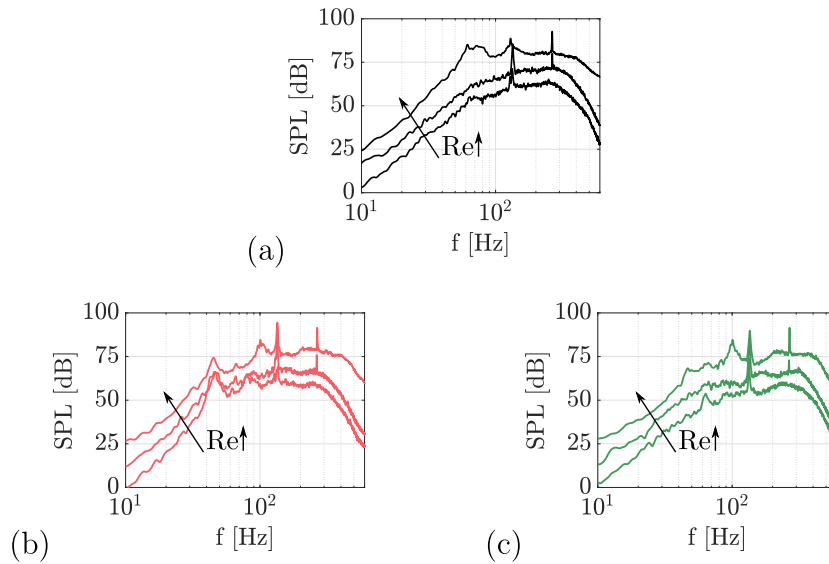
Fig. 4. A-weighted SPL spectra of the different configurations as a function of scaled frequencies, focusing on the *Re* effect. (——) Non-barrier. (——) Barrier *A*. (——) Barrier *B*.
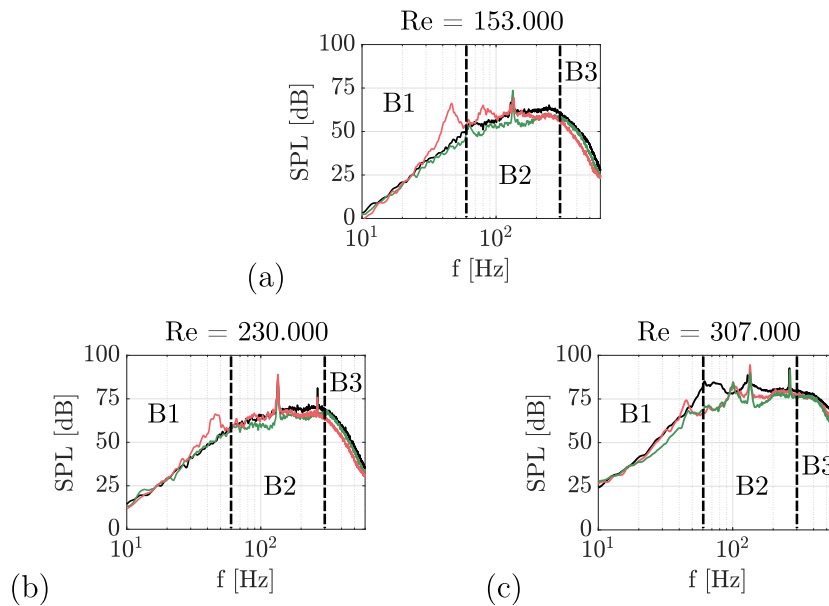

Fig. 5. A-weighted SPL spectra of different configurations at different *Re* as a function of scaled frequencies. (a) *Re* = 153 000. (b) *Re* = 230 000. (c) *Re* = 307 000. (——) Non-barrier. (——) Barrier *A*. (——) Barrier *B*. *B*1, *B*2 and *B*3 are three frequency bands analysed with directivity graphs in Fig. 6.

Table 1
Overall SPL levels measured between 25–600 Hz. Data taken from the A-weighted SPL presented in Fig. 4.

Re	No-bar. [dB]	Bar. *A* [dB]	Bar. *B* [dB]
Low	75	81	72
Medium	84	87	82
High	99	95	93

*B*3 shows a steep drop of the spectra, thus, the low frequency ranges become relevant even if A-weighted levels are taken into consideration. As confirmed in [45,46], the importance of the noise propagation at low frequencies (even lower than 20 Hz) is fundamental to guarantee and preserve health and comfort of neighbouring inhabitants. Lowering the noise levels in these frequency ranges would therefore be beneficial for the surroundings of a train

pass-by. Some further considerations can be made using the Bragg's law. The separation between cylinders is 0.25 W (Fig. 2 (b)), therefore, the central frequency of the band gap $f_{bg} = c/(2 \times 0.25W \times 25) = 227$ Hz (25 represents the scaling factor mentioned above). Thus, in a medium at rest one could expect the lowest band gap of attenuation of acoustic waves in the range 100–300 Hz, which well corresponds with the results shown for the low and medium *Re*. Concerning the high *Re*, an even lower frequency attenuation is induced by barrier *B*, suggesting a possible influence of the barriers on the flow field structures. This last consideration need further investigations and goes beyond the scope of this paper. Nevertheless, it is an important aspect to be confirmed with even higher *Re* simulations, in order to fully understand the evolution of the SPL with an increasing speed.

Fig. 6 shows the OASPL of all cases considered here. Considering Figs. 5 and 6 at the same time, it is clear how barrier *B* brings the
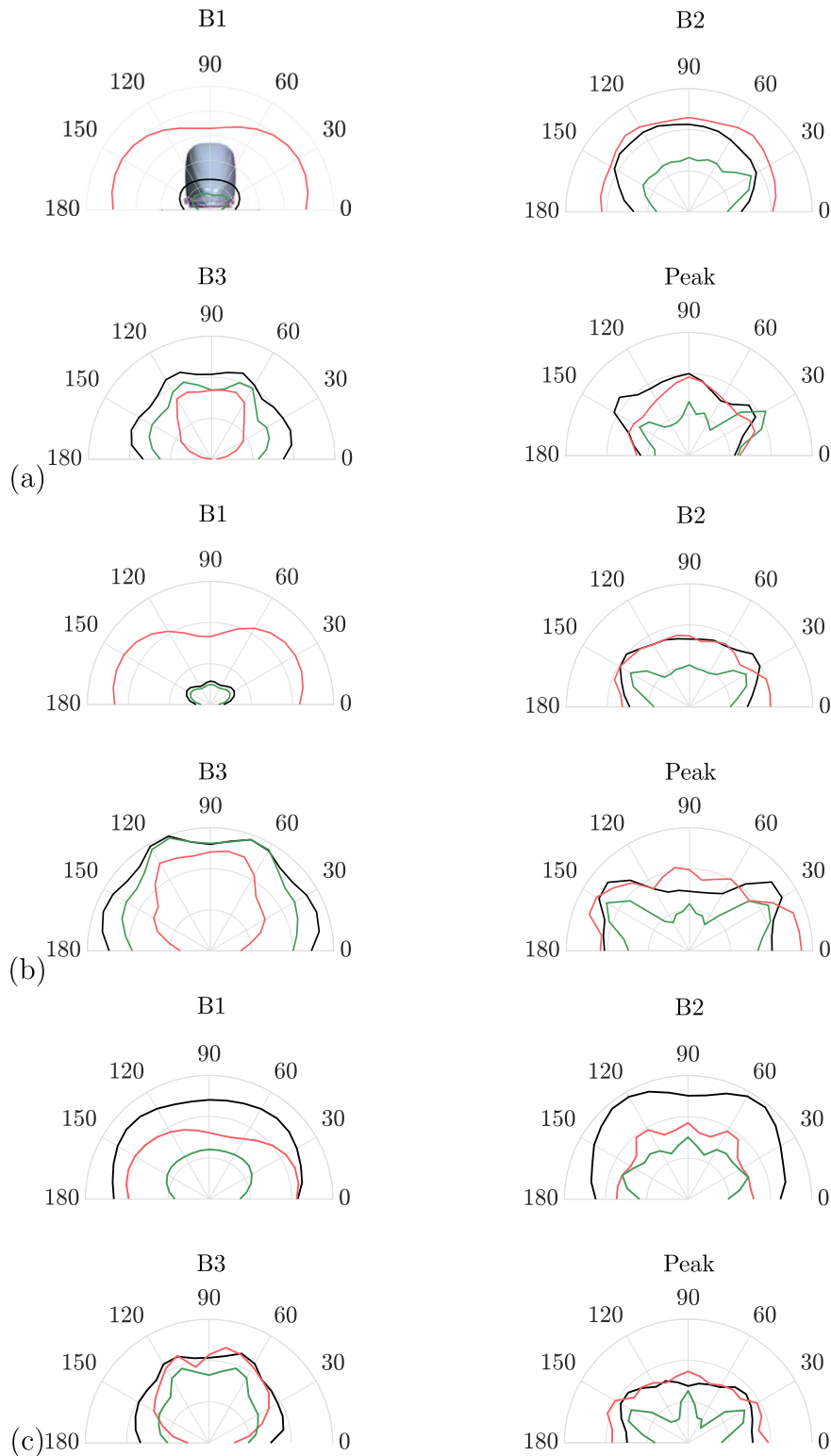
Fig. 6. Overall sound pressure level at different *Re* for different barrier configurations. (a) *Re* = 153 000. (b) *Re* = 230 000. (c) *Re* = 307 000. (——) Non-barriers. (——) Barrier *A*. (——) Barrier *B*. Refer to Fig. 5 for the corresponding band widths *B*1, *B*2 and *B*3. The subfigures labelled with 'Peak' display the noise levels in the frequency band with a 50 Hz bandwidth around the tone at 135 Hz. A circular gray line is drawn every fifth dB.

overall best noise reduction. Only at low and medium *Re* (Fig. 6(a-b)), barrier *A* shows better performance within the *B*3 bandwidth, while, for all other band widths, the cylindrical barriers are consistently more effective. Noteworthy is the impressive (10 dB) reduction observed in *B*2 by barrier *B*. This band is in fact

the most reduced by barrier *B*, consistently across the flow speeds. The distribution of the cylinders, their dimensions and the distances between them, may influence the operational band of the barrier. A parametric study of these variables would be an interesting topic for a future continuation of this work.

As a note to the reader, the presented aeroacoustic results are significant, but they only give information on a limited range of the Reynolds number and the slight asymmetry observed for some of the OASPL in Fig. 6 is probably related to the limited sampling time used. A longer sampling time would have resulted in an unavailable computational cost. Nevertheless, trends and general observation can be extracted but a more comprehensive study, specifically on the topic, needs to be performed to understand the presence (as it has been established for the behaviour of aerodynamic loads) of a threshold, after which the aeroacoustic response stays unchanged.

3.2. Barriers and Reynolds number dependency. Aerodynamic loads characterization

The aerodynamic characteristics and the aerodynamic influence of the screens are reported in this section. Table 2 shows the evolution of the force coefficients and their root mean square (r.m.s.) values along with increasing Re. The force coefficients slowly settle on a plateau at higher speeds, confirming the behaviour described in Ref. [30]. On the other hand, the oscillation level reported by r.m.s. values remains constant with increasing speed. It is more interesting to look at the difference between different geometries. With the help of Fig. 7, one can observe the different trends for the three cases. The Barrier A case consistently shows a 20% higher drag compared to the non-barrier case and a two times higher r.m.s. (C_d), while barrier B shows only a mild drag increase and a very similar r.m.s. level (see Table 2 for the r.m.s. values). Moreover, the drag difference between barrier A and the non-barrier case slightly increases with increasing Re (from 20 to 22%), while the opposite trend is observed for barrier B where the C_d difference decreases with increasing Re (from 5 to 3%). Concerning downforce (negative lift), A shows a consistent higher value (in absolute terms) compared to the other two cases. In particular for $Re = 230\,000 - 307\,000$, barrier A produces a 170% higher downforce while barrier B shows only a 16% increase. This higher downforce is associated with a visibly higher uptrend characterizing the evolution of the vortex core downstream in the wake.

Fig. 8 shows the typical counter-rotating wake vortices characterizing a train wake. The vortex cores and the C_p value projected on the train surface are shown in the picture. The non-barrier case and barrier B present a fairly similar distribution of C_p and topology of the wake cores. On the other hand, the Barrier A case shows a different behavior. Its wake cores remain confined to the space

Table 2
Force values for different configurations.

$Re = 153\,000$	No-bar.	Bar. A	Bar. B
$C_{d(total)}$	0.350	0.421	0.366
$C_{d(shear)}$	0.132	0.151	0.131
r.m.s. ($C_{d(total)}$)	0.006	0.010	0.007
$C_{l(total)}$	−0.088	−0.324	−0.115
r.m.s. ($C_{l(total)}$)	0.020	0.033	0.03
$Re = 230\,000$	No-bar.	Bar. A	Bar. B
$C_{d(total)}$	0.332	0.404	0.342
$C_{d(shear)}$	0.130	0.148	0.130
r.m.s. ($C_{d(total)}$)	0.005	0.011	0.006
$C_{l(total)}$	−0.138	−0.373	−0.16
r.m.s. ($C_{l(total)}$)	0.021	0.033	0.023
$Re = 307\,000$	No-bar.	Bar. A	Bar. B
$C_{d(total)}$	0.319	0.396	0.330
$C_{d(shear)}$	0.130	0.147	0.130
r.m.s. ($C_{d(total)}$)	0.005	0.009	0.005
$C_{l(total)}$	−0.156	−0.388	−0.190
r.m.s. ($C_{l(total)}$)	0.021	0.026	0.018

between the screens contributing to the uptrend discussed later. Moreover, the presence of two strong side vortices, which increase the shear drag by 15% (Table 2, $C_{d(shear)}$), is observed. Looking in particular at Fig. 9, one can observe the clear uptrend of the wake vortex cores. From a previous study performed by the same research group [10], this uptrend was found to be strongly associated with higher downforce. The same is found here, and the presence of this uptrend could possibly be associated with an increase of the ballast flight phenomenon. Barrier B, on the other hand, does not influence the flow in these terms, and no uptrend is observed in the wake cores (see Fig. 9).

3.3. The underbody flow: near-field structures and far-field noise

To complete the visualization of the main flow features, the underbody flow is presented in Figs. 10 and 11. Fig. 10 shows the presence of a strong vortex originating at the nose tip and evolving along the train underbody. All three cases share this feature. Fig. 11 emphasises the dominance of the vortices K in the underbody region. In this last figure, it is observed that the instantaneous flow structures (visualized by the second invariant of the velocity at the magnitude of $Q = 4000$) are distributed along and around the vortex core, presented as a thick solid green line. Another aspect visualized in Fig. 10 is the C_p distribution on the train's nose. The right half of the trains with screens (colored in gray scale) represents the difference in C_p distribution compared to the non-barrier case as $|C_p - C_p^{barA/B}|$. This shows that the barrier B case presents a very similar distribution to the non-barrier case, while a larger portion of the frontal area of the barrier A case is characterized by a larger pressure difference. This also contributes to the drag increase visualized in Fig. 7 and Table 2.

Fig. 12 shows a 2D cut-plane of the swirling vortices forming at the train's pilot sides. The spanwise (the y direction) velocity is investigated by a POD study performed on the plane defined in Fig. 1(c). In Fig. 12, the left plot contains a snapshot of the streamwise velocity taken at $Re = 230\,000$. The dashed gray rectangles indicate the regions post-processed with POD, whose results are shown in the centre frame. In the far right plots of the same picture, a power spectral density (PSD) plot of the first POD mode is shown. Interestingly, the first (most energetic) mode shows structures moving with the same frequency, regardless of the barrier type and the Reynolds number. This indicates a recursive flow dynamics, possibly associated with the tonal peak shown in Figs. 4 and 5. As discussed in Section 3.1, a fixed peak was observed in the far-field at 135 Hz, which corresponds to the double of the frequency found in the PSD plot of the first POD mode shown in Fig. 12. In order to relate these two frequencies to each other, note that the Lighthill stress tensor T_{ij} [47,48] is defined as:

$$T_{ij} = \rho u_i' u_j' + (p' - c_0^2 \rho')\delta_{ij} - \sigma_{ij}. \tag{1}$$

The spatial derivatives in T_{ij} represent quadrupole noise sources. Note that T_{ij} at low-Mach numbers mainly depends on the product between velocity perturbations, the first term on the right hand side of the equation above, assuming that the flow is isentropic and that the viscous effect is small. Therefore, the fluctuations of the streamwise velocity field at a specific frequency would generate noise (visible in the far-field spectrum) at the double of this frequency. Having said this, the present authors speculate that the first mode, individuated by the POD analysis, is strongly connected with the tonal peak observed in the far-field noise results. This would partly explain the previous experimental results, nicely reported in Ref. [15], where the authors found constant tonal peaks (with increasing Re) attributable to the front lower part of a similar train model.
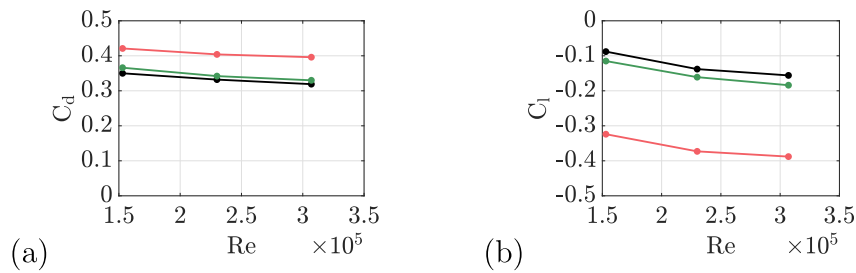
Fig. 7. Trend of the forces with increasing *Re*. (──) Non-barrier. (──) Barrier *A*. (──) Barrier *B*.
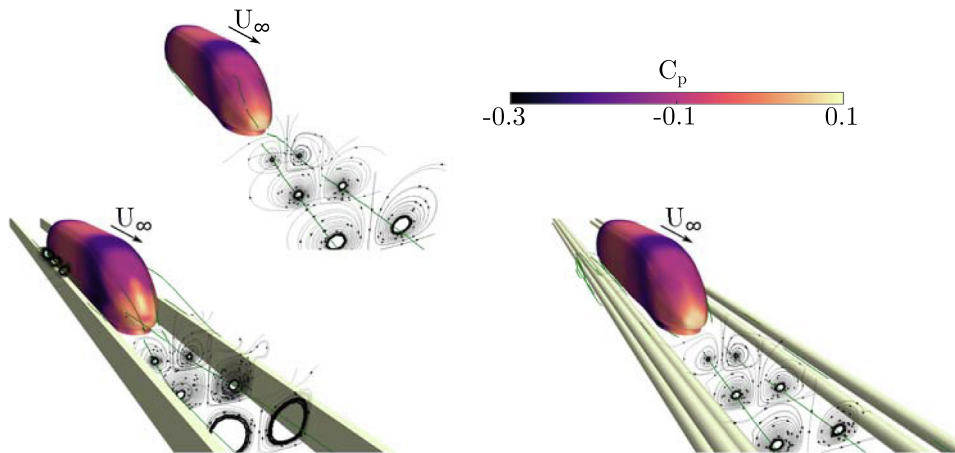

Fig. 8. The wake structures and vortex cores for the three barrier cases. The vortex cores are colored in gray and a zoom of the underbody vortex is provided. The left half of the train surface is colored by the coefficient of pressure C_p. The right half of the train surface cases (bar A and B) show the C_p differences compared to the non-barrier case. $Re = 230\,000$.
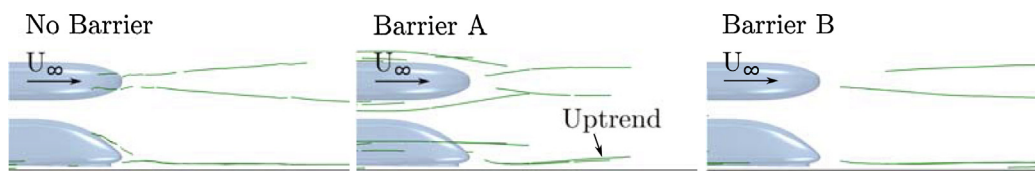

Fig. 9. The wake vortex core trend for the three barrier cases. The vortex cores are colored in green. $Re = 230\,000$.
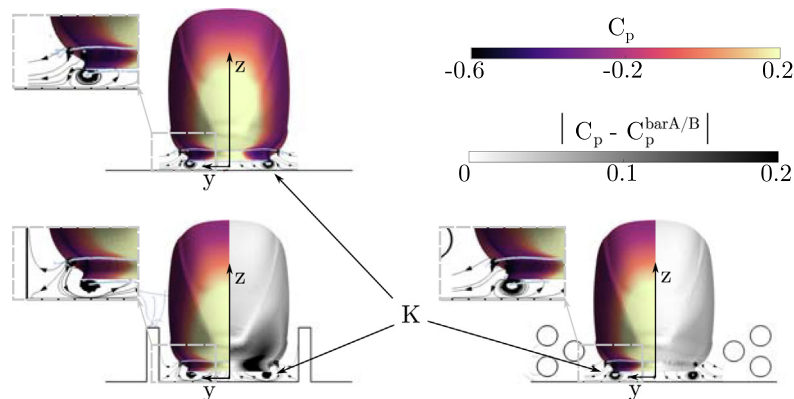

Fig. 10. The underbody pair of vortices K and vortex cores for the three barrier cases. The vortex cores are colored in gray. The train surface is colored by the coefficient of pressure C_p. $Re = 230\,000$.

The same procedure is applied to the streamwise component (in the *x* direction) of the flow velocity. Fig. 13 clearly shows a dependency of this component with the Reynolds number. In particular,

the frequency peaks of the POD temporal coefficient, which are associated with the most energetic mode, shift to higher frequencies with increasing *Re*, keeping the non-dimensional frequency
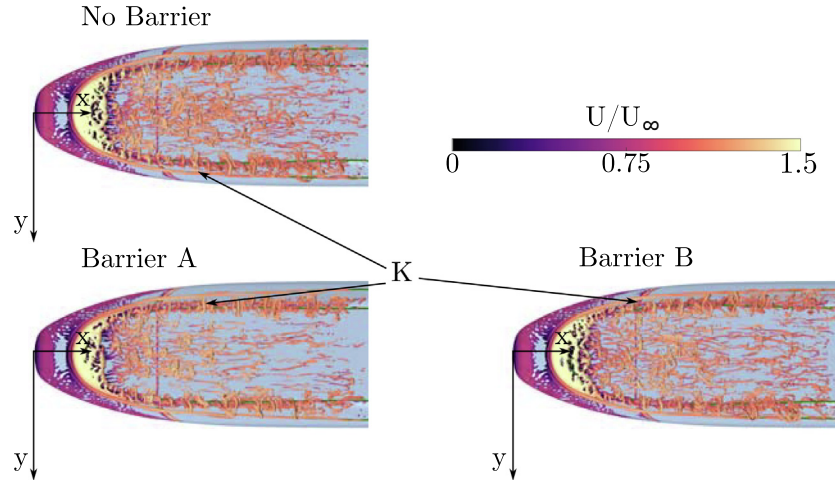
Fig. 11. Flow structures at the underbody for the three cases. The side swirling vortices are named K. The structures are visualized by the second invariant of the velocity at the magnitude of $Q = 4000$. The structures are colored by the averaged normalized streamwise velocity. The vortex cores are colored in green. $Re = 230\,000$.
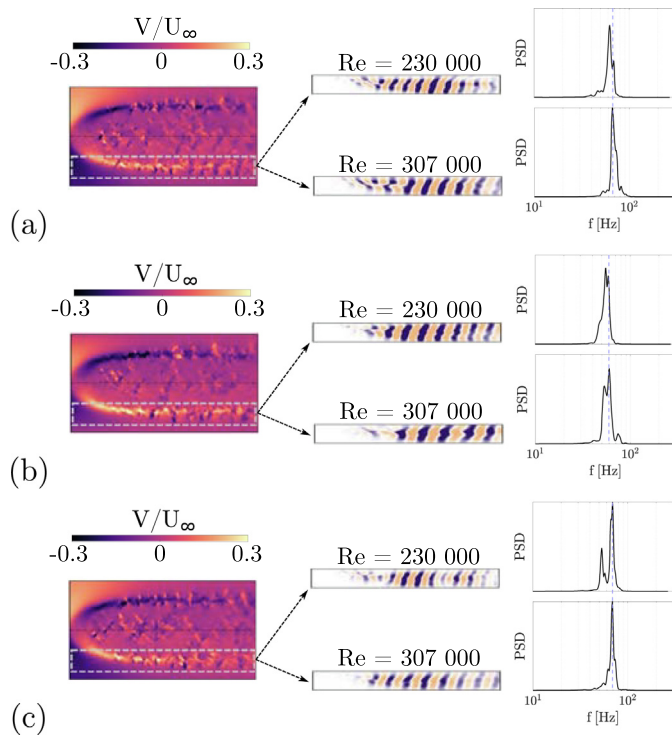

Fig. 12. The most energetic mode extracted by a zonal proper orthogonal decomposition (POD) for the spanwise (the y direction) component of the velocity field. Left, a snapshot of the sampling plane lying at $z = 0$ (see Fig. 1(c) for the plane location). Centre, the first POD mode extracted from the dashed area. Right, power spectral density (PSD) of the temporal coefficient associated with each respective POD mode. (a) Non-barrier case. (b) Barrier A case. (c) Barrier B case.

$F^+ = fW/U_\infty$ constant. All three cases present a similar behaviour, showing a pair of swirling vortices which are characterized by a Re-independent spanwise velocity component and a Re-dependent streamwise component, the former being connected to the tonal peak observed in the far-field.

The relatively insensitive dependency of the spanwise velocity component on the streamwise inflow speed is supported by Fig. 14, which shows how the non-normalized velocity component changes with increasing Re. The field of the spanwise velocity component V shows a very slight dependency on Re. This effect is

reconnected to the reasons and results shown above. On the other hand, the streamwise component of the underbody velocity drastically changes with the increasing inflow speed, supporting the visualization of Figs. 12 and 13.

To further confirm the presence of the fixed-frequency vortex dynamics in the near field, the impermeable ground surface is analysed in Fig. 15. This figure shows the acoustic response of the ground surface and the spatial distribution of the peak frequency at 135 Hz at $Re = 153\,000$, $230\,000$ and $307\,000$. Two streaks (colored in orange) are observed, corresponding to the shape and position of the swirling vortices K visualized in Fig. 10 and 11. They extend on both sides of the train underbody from the nose tip downwards. The higher Re leads to a more prominent trace on the ground surface, although at all Re the marks are clearly visible.

To summarize this last section, the lateral component of the underbody swirling vortices is given by the sharp curved frontal edge, while the streamwise component is dominated by the high-speed flow generated in the gap between the train and ground. Thus, the streamsise component of the vorticies K is mostly influenced by the inflow speed, while the spanwise component remains possibly defined by the geometrical shape of the frontal edge. In the present work, it is identified that the particular curvature triggers the spanwise motion that does not change with the inflow (streamwise) velocity. The spanwise motion develops the same type of flow structures, which are supposedly connected to the far-field noise peak. For clarity, the authors only investigated this particular model. In the future work, a specifically designed geometry shall be used to parameterize the sharp frontal curvature and study its influence on the far-field noise.

4. Conclusions

The impacts of different noise barriers on the aeroacoustic signature of high-speed trains is studied in this work. To explore the details of the noise generation and propagation affected by the barriers, a compressible improved-detached-delayed eddy (IDDES) method based on the Spalart–Allmaras turbulence model is used to simulate the flows induced by the train and barriers at a range of Reynolds numbers. The train model is a simplified ICE3 model with a single car. The car is symmetric with respect to the centre. Complex details of the geometry have been removed, and the bogie cavities have been filled, in order to save computational resources but also to reproduce a modern streamlined train model. In partic-
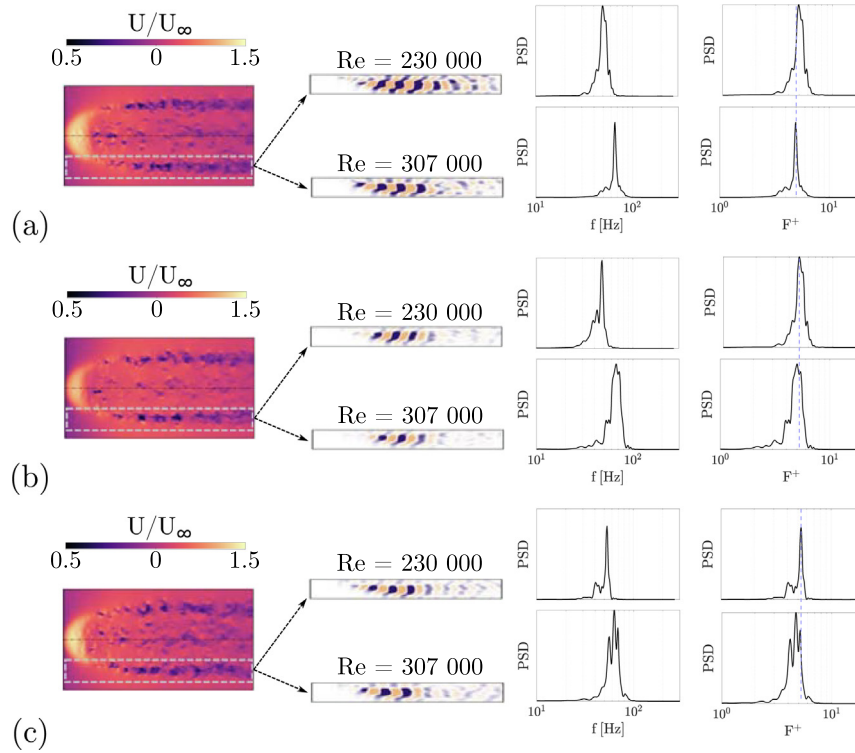
Fig. 13. The most energetic mode extracted by a zonal proper orthogonal decomposition (POD) for the streamwise (in the *x* direction) component of the velocity field. Left, a snapshot of the sampling plane lying at *z* = 0 (see Fig. 1(c) for the plane location). Centre, the first POD mode extracted from the dashed area. Right, power spectral density (PSD) of the temporal coefficient associated with each respective POD mode. (a) Non-barrier case. (b) Barrier *A* case. (c) Barrier *B* case.
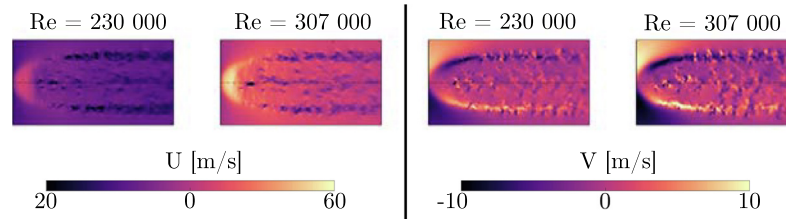

Fig. 14. Snapshots of non-normalized velocity components at different *Re* for the non-barrier case. Left, streamwise (*x* direction) velocity component. Right, spanwise (*y* direction) velocity component.

ular, three general noise barrier configurations are constructed and investigated: non-barrier, vertical closed at the ground barrier (barrier *A*) and sonic-crystal-inspired barrier (barrier *B*). All cases have been studied at $Re = 153\,000$, $230\,000$ and $307\,000$.

The results can be divided into three main parts. (i) The aeroacoustic signature of the train model under three different scenarios corresponding to the non-barrier and two different noise barrier cases is shown. (ii) The influences of the noise barriers on the global aerodynamic forces is analysed. (iii) An attempt to explore the connection between the near-field turbulent flow structures and the far-field noise peaks is described. More in detail, (i) the *B* barrier case shows the overall best efficiency in terms of the noise reduction. (ii) In addition, barrier *B* does not critically affect the aerodynamic performance of the train model. On the other hand, barrier *A* not only performs worse with increasing *Re* but also significantly affects the train aerodynamics with an unacceptable 20% drag increase. (iii) A tonal peak at 135 Hz (in the real scale) is consistently observed in the far-field acoustic spectra, across different *Re* and different barrier configurations. A modal analysis based on proper orthogonal decomposition (POD) suggests as a viable

explanation that the acoustic phenomenon is brought by the swirling vortex pair detaching from the bottom sharp edge of the train. The roll-up of the vortices gives rise to distinct and constant spanwise velocity fluctuations, which are defined by half of the frequency of the previously mentioned far-field peak. Based on the analysis of the Lighthill stress tensor, one can attribute the flow velocity fluctuations to the acoustic pressure fluctuations and hypothesise a possible connection between them.

This study is the first work, to the knowledge of the authors, that numerically analyses the aeroacoustic signature of an entire train car at significantly high Reynolds numbers. As a future work, the dimension and distribution of the sonic crystals can be optimized to exploit their features. A fundamental study of a simplified geometry characterized by a curved sharp leading edge will possibly confirm and explain in a more detailed way about the connection between the far-field spectral peak and the shear swirling vortices that are present in the underbody flow. From a more industrial and practical point of view, the presence of a threshold *Re*, after which the aeroacoustic response could stay unchanged, should be also investigated.
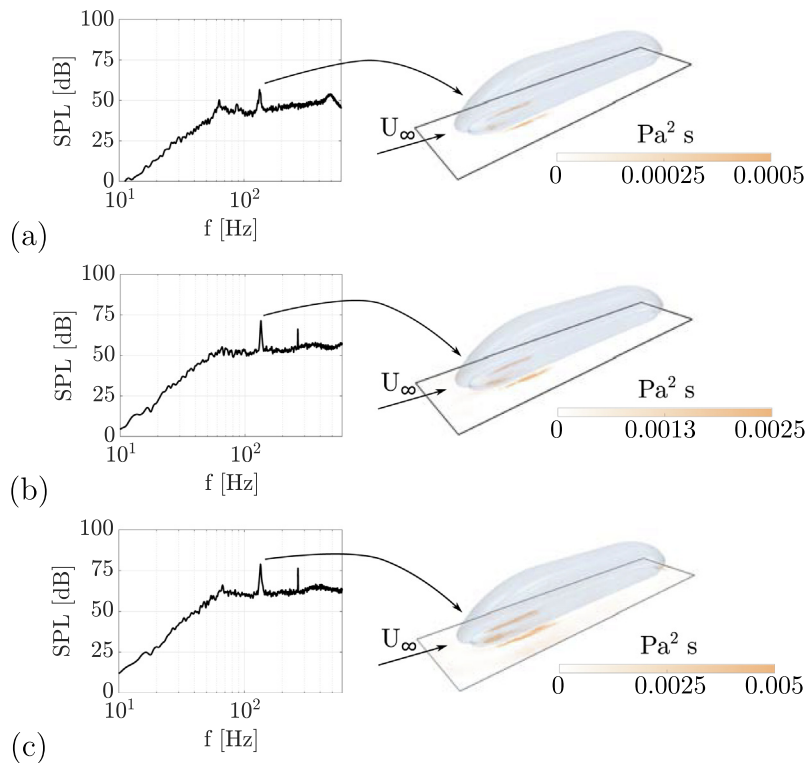
Fig. 15. Energy distribution of a specific frequency on the ground under the train model. Left, A-weighted sound pressure level of the emitted noise by the ground solid surface. Right, the energy distribution of the peak at 135 Hz. (a) $Re = 153\,000$, (b) $Re = 230\,000$, (c) $Re = 307\,000$.

Declaration of Competing Interest

The authors declare that they have no known competing financial interests or personal relationships that could have appeared to influence the work reported in this paper.

Acknowledgements

References

[1] Baker CJ. A review of train aerodynamics. Part 1 – Fundamentals. Aeronaut J 2014;118:201–28.
[2] Baker CJ. A review of train aerodynamics. Part 2 - Applications. Aeronaut J 2014;118:345–82.
[3] Bell JR, Burton D, Thompson MC, Herbst AH, Sheridan J. Moving model analysis of the slipstream and wake of a high-speed train. J Wind Eng Ind Aerodyn 2015;136:127–37.
[4] Bell JR, Burton D, Thompson MC, Herbst AH, Sheridan J. Moving model analysis of the slipstream and wake of a high-speed train. J Wind Eng Ind Aerodyn 2015;136:127–37.
[5] Bell JR, Burton D, Thompson MC, Herbst AH, Sheridan J. Flow topology and unsteady features of the wake of a generic high-speed train. J Fluids Struct 2016;61:168–83.
[6] Krajnović S, Ringqvist P, Nakade K, Basara B. Large eddy simulation of the flow around a simplified train moving through a crosswind flow. J Wind Eng Ind Aerodyn 2012;110:86–99.
[7] Krajnović S. Shape optimization of high-speed trains for improved aerodynamic performance. Proc Inst Mech Eng Part F J Rail Rapid Transit 2009;223:439–52.
[8] Wang J, Minelli G, Dong T, Chen G, Krajnović S. The effect of bogie fairings on the slipstream and wake flow of a high-speed train. An IDDES study, Wind Eng Ind Aerodyn; 2019 [in print].
[9] Dong T, Liang X, Krajnović S, Xiong X, Zhou W. Effects of simplifying train bogies on surrounding flow and aerodynamic forces. J Wind Eng Ind Aerodyn 2019;191:170–82.

[10] Dong T, Minelli G, Wang J, Liang X, Krajnović S. The effect of ground clearance on the aerodynamics of a generic high-speed train. J Fluids Struct 2020;95:102990.
[11] Fremion N, Vincent N, Jacob M, Robert G, Louisot A, Guerrand S. Aerodynamic noise radiated by the intercoach spacing and the bogie of a high-speed train. J Sound Vib 2000;231:577–93.
[12] Nagakura K. Localization of aerodynamic noise sources of Shinkansen trains. J Sound Vib 2006;293:547–56.
[13] Kurita T. Development of external-noise reduction technologies for Shinkansen high-speed trains. J Environ Eng 2011;6:805–19.
[14] Paradot N, Masson E, Poisson F, Grégoire R, Guilloteau E, Touil H, Sagaut P. Aero-acoustic methods for high-speed train noise prediction. In: WCRR'08.
[15] Lauterbach A, Ehrenfried K, Loose S, Wagner C. Microphone array wind tunnel measurements of Reynolds number effects in high-speed train aeroacoustics. Int J Aeroacoust 2012;11:411–46.
[16] Sueki T, Ikeda M, Takaishi T. Aerodynamic Noise Reduction using Porous Materials and their Application to High-speed Pantographs. Quart Rep RTRI 2009;50:26–31.
[17] Zhu J, Hu Z, Thompson DJ. Flow behaviour and aeroacoustic characteristics of a simplified high-speed train bogie. Proc Inst Mech Eng Part F J Rail Rapid Transit 2016;230:1642–58.
[18] Pignier NJ, O'Reilly CJ, Boij S. Aerodynamic and aeroacoustic analyses of a submerged air inlet in a low-Mach-number flow. Comput Fluids 2016;133:15–31.
[19] Zhu JY, Hu ZW, Thompson DJ. The flow and flow-induced noise behaviour of a simplified high-speed train bogie in the cavity with and without a fairing. Proc Inst Mech Eng Part F J Rail Rapid Transit 2018;232:759–73.
[20] Minelli G, Yao H-D, Andersson N, Höstmad P, Forssén J, Krajnović S. An aeroacoustic study of the flow surrounding the front of a simplified ICE3 high-speed train model. Appl Acoust 2020;160:107125.
[21] Yao H-D, Davidson L, Eriksson LE. Noise radiated by low-Reynolds number flows past a hemisphere at Ma = 0.3. Phys Fluids 2017;29:0–14.
[22] Rahier G, Prieur J, Vuillot F, Lupoglazoff N, Biancherin A. Investigation of integral surface formulations for acoustic post-processing of unsteady aerodynamic jet simulations. Aerosp Sci Technol 2004;8:453–67.
[23] Freund JB, Lele SK, Moin P. Calculation of the radiated sound field using an open Kirchhoff surface. AIAA J 1996;34:909–16.
[24] Peiró-Torres M, Redondo J, Bravo J, Pérez JS. Open noise barriers based on sonic crystals. Adv Noise Control Transp Infrastruct Transport Res Procedia 2016;18:392–8.
[25] Kushwaha MS. Stop-bands for periodic metallic rods: sculptures that can filter the noise. Appl Phys Lett 1997;70:3218–20.
[26] Sanchez-Perez JV, Rubio C, Martinez-Sala R, Sanchez-Grandia R, Gomez V. Acoustic barriers based on periodic arrays of scatterers. Appl Phys Lett 2002;81:5240–2.

[27] Castiñeira-Ibáñez S, Rubio C, Romero-García V, Sánchez-Pérez JV, García-Raffi LM. Design, manufacture and characterization of an acoustic barrier made of multi-phenomena cylindrical scatterers arranged in a fractal-based geometry. Arch Acoust 2012;37:455–62.

[28] Rubio C, Castiñeira-Ibáñez S, Sánchez-Pérez, JV, Candelas P, Belmar F, Uris A. Open acoustic barriers: a new attenuation mechanism. In: Advances in Noise Analysis, Mitigation and Control, InTech; 2016.

[29] Thota M, Wang KW. Reconfigurable origami sonic barriers with tunable bandgaps for traffic noise mitigation. J Appl Phys 2017;122:154901.

[30] CEN: European Committee for Standardization, Railway applications. Aerodynamics. Requirements and test procedures for aerodynamics on open track, NSAI standards; 2013.

[31] STAR-CCM+,https://mdx.plm.automation.siemens.com/star-ccm-plus; 2018.

[32] Shur ML, Spalart PR, Strelets MK, Travin AK. A hybrid RANS-LES approach with delayed-DES and wall-modelled LES capabilities. Int J Heat Fluid Flow 2008;29:1638–49.

[33] Spalart P, Allmaras S. A one-equation turbulence model for aerodynamic flows. In: 30th Aerospace sciences meeting and exhibit, aerospace sciences meetings. American Institute of Aeronautics and Astronautics; 1992.

[34] Zhang J, Li JJ, Tian HQ, Gao GJ, Sheridan J. Impact of ground and wheel boundary conditions on numerical simulation of the high-speed train aerodynamic performance. J Fluids Struct 2016;61:249–61.

[35] Fragner MM, Deiterding R. Investigating side-wind stability of high speed trains using high resolution large eddy simulations and hybrid models. Comput Methods Appl Sci 2018;45:223–41.

[36] Wang S, Burton D, Herbst A, Sheridan J, Thompson MC. The effect of bogies on high-speed train slipstream and wake. J Fluids Struct 2018;83: 471–89.

[37] Brentner KS, Farassat F. Analytical comparison of the acoustic analogy and Kirchhoff formulation for moving surfaces. AIAA J 1998;36:1379–86.

[38] Brentner K. Numerical algorithms for acoustic integrals – The devil is in the details. In: 2nd AIAA/CEAS aeroacoustics conference.

[39] Ahrens J, Andersson C, Höstmad P, Kropp W. Tutorial on scaling of the discrete fourier transform and the implied physical units of the spectra of time-discrete signals. 148th Convention of the AES, e-Brief 56; 2020.

[40] Lumley JL. Stochastic tools in turbulence – applied mathematics and mechanics. New York: Academic Press; 1970.

[41] Sirovich L. Turbulence and the dynamics of coherent structures. Part i: coherent structures. Quart Appl Math 1987;XLV:561–71.

[42] Minelli G, Krajnović S, Basara B, Noack BR. Numerical investigation of active flow control around a generic truck A-Pillar. Flow Turbul Combust 2016;97:1235–54.

[43] Minelli G, Adi Hartono E, Chernoray V, Hjelm L, Krajnović S. Aerodynamic flow control for a generic truck cabin using synthetic jets. J Wind Eng Ind Aerodyn 2017;168:81–90.

[44] Minelli G, Adi Hartono E, Chernoray V, Hjelm L, Krajnović S, Basara B. Validation of PANS and active flow control for a generic truck cabin. J Wind Eng Ind Aerodyn 2017;171:148–60.

[45] Møller H, Pedersen CS. Hearing at low and infrasonic frequencies. Noise Health 2004;6:37–57.

[46] Møller H, Pedersen CS. Low-frequency noise from large wind turbines. J Acoust Soc Am 2011;129:3727–44.

[47] Lighthill MJ, Newman MHA. On sound generated aerodynamically I. General theory. Proc R Soc Lond Ser A Math Phys Sci 1952;211:564–87.

[48] Lighthill MJ. On sound generated aerodynamically II. Turbulence as a source of sound. Proc R Soc Lond Ser A Math Phys Sci 1954;222:1–32.